Modeling the local excitation fluence rate and fluorescence emission in absorbing and strongly scattering multilayered media

Dmitry Yudovsky and Laurent Pilon*

Henry Samueli School of Engineering and Applied Science, Department of Mechanical and Aerospace Engineering,
Biomedical Inter-Department Program, University of California, Los Angeles,
Los Angeles, California 90095-1597, USA

*Corresponding author: pilon@seas.ucla.edu

Received 2 March 2010; revised 2 July 2010; accepted 22 August 2010;
posted 24 August 2010 (Doc. ID 124827); published 26 October 2010

We present computationally efficient and accurate semiempirical models of light transfer for real-time analysis of multilayer fluorescing media exposed to normally incident excitation light. The model accounts for absorption and strong forward scattering as well as for internal reflection at the interface between the medium and the surrounding air. The absorption and scattering coefficients are assumed to be constant with depth; the fluorophore concentration is considered piecewise constant. The refractive index ranges from 1.0 to 2.0, and the transport single scattering albedo between 0.50 and 0.99. First, simple analytical expressions for local excitation fluence rate within the medium and surface fluorescence intensity emerging from its surface were derived from the two-flux approximation. Then, parameters appearing in the analytical expression previously derived were fitted to match results from more accurate Monte Carlo simulations. A single semiempirical parameter was sufficient to relate the diffuse reflectance of the medium at the excitation wavelength to the local excitation fluence rate within the medium and to the surface fluorescence emission intensity. The model predictions were compared with Monte Carlo simulations for local fluence rate and total surface fluorescence emission from (i) homogeneous semi-infinite fluorescing media, (ii) media with a semi-infinite fluorescing layer beneath a nonfluorescing layer, and (iii) media with a finite fluorescing layer embedded in a nonfluorescing semi-infinite layer. The model predictions of the local excitation fluence rate and of the total surface fluorescence emission fell to within 5% of predictions by Monte Carlo simulations for single scattering albedo greater than 0.90. The current model can be used for a wide range of applications, including noninvasive diagnosis of biological tissue. © 2010 Optical Society of America

OCIS codes: 000.4430, 010.5620, 170.6280, 230.4170, 170.6510, 110.7050.

1. Introduction

Fluorescence is the physical phenomenon in which light is emitted by a substance as a result of excited electrons returning to their ground states after the absorption of excitation light [1,2]. Fluorescing substances (fluorophores) are characterized by their quantum yield, their fluorescence lifetime(s), and their emission wavelengths. Emission occurs over a wide spectral range and at wavelengths longer than the excitation wavelength. The quantum yield is the ratio of the number of photons emitted to the number of photons absorbed, whereas the fluorescence lifetime is the average time the electrons spend in their excited states [1,2]. Biological tissues contain several endogenous fluorophores, such as nicotinamide adenine dinucleotide (NAD or NADH), aromatic amino acids such as tryptophan, and structural proteins, such as collagen and elastin [3]. The optical properties of these fluorophores are sensitive to the environment and the metabolic state of the tissue, making fluorescence spectroscopy a valuable tool to study the health of biological tissues [1,2,4–6].

0003-6935/10/316072-13$15.00/0

Steady-state fluorescence spectroscopy has been widely used to monitor biological tissues [1,4–11]. It consists of exposing the medium of interest to collimated or diffuse excitation light (typically UV) and measuring the fluorescence intensity emerging from the tissue surface. Fluorescence spectroscopy typically involves either emission spectra or excitation spectra measurements. Fluorescence emission spectra measurements consist of measuring the fluorescence intensity over a range of wavelengths for a fixed excitation wavelength. On the other hand, excitation spectra measurements consist of measuring the fluorescence intensity at a particular wavelength for a certain range of excitation wavelengths. Fluorophores are typically present throughout biological tissues, and the fluorescent light is absorbed and scattered before emerging from the tissue. Thus, measurements of fluorescence intensity detected at the tissue surface depend on the optical properties of both the fluorophores and the medium. Intrinsic fluorescence is defined as the fluorescence intensity emitted by the tissue's fluorophores after removing the effects of tissue scattering and absorption.

Analytical approaches to recovering intrinsic fluorescence spectra have been based on approximate solutions of the radiative transfer equation, such as the Beer–Lambert law [12], diffusion approximation [12–14], and the two-flux approximation [15,16]. Correction factors for the boundary conditions in the diffusion and two-flux approximations have been developed to account for index mismatch at the boundary between the air and the medium [17,18]. However, the diffusion approximation fails in media when absorption is significant, and two-flux approximation fails if scattering is strongly anisotropic and weak [17,18]. Instead, semiempirical models have been developed that combine the simplicity of approximate solutions and the accuracy of Monte Carlo simulations [11,16,19]. Typically, the algebraic form of an approximate solution is used along with empirical parameters provided in a lookup table obtained from Monte Carlo simulations. Gardner *et al.* [12] developed a heuristic model for the local fluence rate and fluorescence escape function for a homogeneous, semi-infinite medium with a specified refractive index using six semiempirical parameters expressed as a function of the diffuse reflectance.

Intrinsic fluorescence spectroscopy has been typically performed on internal organs with the assumption that they were homogeneous [4–6]. However, this assumption may not accurately predict fluorescence from tissue in which fluorophore distribution is multilayered. Such an instance can arise if the tissue is stained with a fluorescent dye that (i) significantly alters the fluorescence properties of a layer of tissue but (ii) does not significantly affect tissue scattering or absorption [20–24]. This can be modeled as a two-layer fluorescing medium in which fluorescence is stronger in the top layer than in the bottom. Alternatively, internal malignancies, such as tumors, can be stained intravenously with contrast agents to create a layer of strong fluorescence within healthy tissue that does not fluoresce significantly [25,26]. This situation can be modeled as a three-layer medium such that a strongly fluorescing layer representing the tumor exists between two weakly fluorescing layers. The objective of this study is to develop a simple and accurate expression for the excitation fluence rate and the total fluorescence emission intensity of multilayer fluorescing media. Similar to previous studies, the absorption and scattering coefficients of the medium were assumed to be constant with depth. However, fluorophore concentration was considered to vary stepwise with depth to simulate fluorescence from multilayered tissue. Furthermore, the index of refraction of the medium was treated as a parameter varying between 1.0 and 2.0. This model can be combined with an inverse method to determine the tissue's intrinsic fluorescence coefficient from the measured fluorescence emission of biological tissue.

2. Background

A. Radiative Transfer Equation

The transport of excitation light in absorbing and scattering media is governed by the steady-state radiative transfer equation (RTE). The excitation intensity I_{λ_x} at wavelength λ_x in direction $\hat{s}$ and at location $\hat{r}$ satisfies the steady-state RTE expressed as [27]

$$\hat{s}\cdot\nabla I_{\lambda_x}(\hat{r},\hat{s}) = -\mu_{a,\lambda_x} I_{\lambda_x}(\hat{r},\hat{s}) - \mu_{s,\lambda_x} I_{\lambda_x}(\hat{r},\hat{s}) + \frac{\mu_{s,\lambda_x}}{4\pi} \times \int_{4\pi} I_{\lambda_x}(\hat{r},\hat{s}_i)\Phi_{\lambda_x}(\hat{s}_i,\hat{s})\mathrm{d}\Omega_i, \quad (1)$$

where μ_{a,λ_x} and μ_{s,λ_x} are the linear absorption and scattering coefficients, respectively. The scattering phase function, denoted by $\Phi_{\lambda_x}(\hat{s},\hat{s}_i)$, represents the probability that radiation propagating into the elementary solid angle $\mathrm{d}\Omega_i$ around incident direction $\hat{s}_i$ will be scattered in direction $\hat{s}$.

Moreover, a similar equation can be written for the transport of fluorescent light at wavelength λ_f emitted by fluorophores present within the medium [27]:

$$\hat{s}\cdot\nabla I_{\lambda_f}(\hat{r},\hat{s}) = -\mu_{a,\lambda_f} I_{\lambda_f}(\hat{r},\hat{s}) - \mu_{s,\lambda_f} I_{\lambda_f}(\hat{r},\hat{s}) + \frac{\mu_{s,\lambda_f}}{4\pi} \times \int_{4\pi} I_{\lambda_f}(\hat{r},\hat{s}_i)\Phi_{\lambda_f}(\hat{s}_i,\hat{s})\mathrm{d}\Omega_i + \frac{\gamma_{xf}(\hat{r})G_{\lambda_x}(\hat{r})}{4\pi}. \quad (2)$$

The last term in Eq. (2) represents fluorescence emission at wavelength λ_f stimulated by the excitation light at wavelength λ_x. The term G_{λ_x} is the excitation fluence rate expressed as

$$G_{\lambda_x}(\hat{r}) = \int_{4\pi} I_{\lambda_x}(\hat{r}, \hat{s}) \mathrm{d}\Omega. \quad (3)$$

The intrinsic fluorescence coefficient $\gamma_{xf}(\hat{r})$ is the product of (i) the fluorophore's molar absorption coefficient at excitation wavelength λ_x denoted by ϵ_{f,λ_x}, (ii) its quantum yield at excitation wavelength λ_x and emission wavelength λ_f denoted by $\mathrm{QY}_{xf}(\hat{r})$, and (iii) its molar concentration at location $\hat{r}$ in the tissue denoted by $M(\hat{r})$, i.e., $\gamma_{xf}(\hat{r}) = \epsilon_{f,\lambda_x}\mathrm{QY}_{xf}(\hat{r})M(\hat{r})$. The fluorophore's molar absorption coefficient ϵ_{f,λ_x} and the molar concentration M have units of $\mathrm{cm}^{-1}/(\mathrm{mole/cm}^3)$ and $\mathrm{mole/cm}^3$, respectively, while the quantum yield is unitless [1]. The fluorophore's molar absorption coefficient ϵ_{f,λ_x} can be measured *in vitro* for a dilute solution of the endogenous fluorophore at a known concentration [1].

The Henyey–Greenstein scattering phase function [28] has been used extensively in tissue optics [29–31] and computer animation [32] to account for the anisotropic nature of scattering in tissue. At arbitrary wavelength λ, it is expressed as [28]

$$\Phi_\lambda(\hat{s}_i, \hat{s}) = \frac{1 - g_\lambda}{[1 + g_\lambda^2 - 2g_\lambda \cos\Theta]^{3/2}}, \quad (4)$$

where Θ is the angle between directions $\hat{s}$ and $\hat{s}_i$, and g_λ is the so-called Henyey–Greenstein asymmetry factor.

Light propagation in strongly scattering media can be characterized by the transport single scattering albedo $\omega_{tr,\lambda}$ and the transport total extinction coefficient $\beta_{tr,\lambda}$, respectively, defined as [27]

$$\omega_{tr,\lambda} = \frac{\mu_{s,tr,\lambda}}{\mu_{s,tr,\lambda} + \mu_{a,\lambda}} = \frac{\mu_{s,\lambda}(1 - g_\lambda)}{\mu_{s,\lambda}(1 - g_\lambda) + \mu_{a,\lambda}},$$
$$\beta_{tr,\lambda} = \mu_{s,\lambda}(1 - g_\lambda) + \mu_{a,\lambda}. \quad (5)$$

Here, $\mu_{s,tr,\lambda} = \mu_{s,\lambda}(1 - g_\lambda)$ is the transport scattering coefficient that accounts for both the magnitude and the anisotropy of the scattering phenomenon [27].

B. Two-Flux Approximation of Collimated Excitation Light Transport

Approximate solutions to the RTE are commonly used, since explicit solutions are available only for a limited number of cases [27,33]. The so-called two-flux approximation is derived under the assumptions that (i) the medium is plane parallel, (ii) light transfer is one-dimensional, and (iii) the intensity is isotropic but different in the upper and lower hemispheres. Then, the RTE simplifies to a set of two coupled linear ordinary differential equations [27,34] originally presented by Kubelka [35]:

$$\frac{dF^+_{\lambda_x}}{dz} = -a_{\lambda_x} S_{\lambda_x} F^+_{\lambda_x} + S_{\lambda_x} F^-_{\lambda_x} + S_{1,\lambda_x} F_{c,\lambda_x}, \quad (6)$$

$$\frac{dF^-_{\lambda_x}}{dz} = -S_{\lambda_x} F^+_{\lambda_x} + a_{\lambda_x} S_{\lambda_x} F^-_{\lambda_x} - S_{2,\lambda_x} F_{c,\lambda_x}, \quad (7)$$

where $F_{c,\lambda_x}(z)$ is a source term associated with the unattenuated collimated incident light, and $F^+_{\lambda_x}$ and $F^-_{\lambda_x}$ are the diffuse excitation fluxes propagating into the positive and negative z directions, respectively. Here, z is the depth inside the medium defined from the medium–air interface as illustrated in Fig. 1(a). These diffuse fluxes at arbitrary wavelength λ can be expressed in terms of the local intensity $I_{\lambda_x}(z, \theta)$ as [34]

$$F^+_\lambda(z) = 2\pi \int_0^{\pi/2} I_\lambda(z, \theta) \cos\theta \sin\theta \mathrm{d}\theta,$$

$$F^-_\lambda(z) = -2\pi \int_{\pi/2}^{\pi} I_\lambda(z, \theta) \cos\theta \sin\theta \mathrm{d}\theta. \quad (8)$$

The polar angle θ was taken relative to the inward surface normal as illustrated in Fig. 1(a). The coefficients K_{λ_x} and S_{λ_x} are the absorption and scattering coefficients for diffuse fluxes, respectively, and $a_{\lambda_x} = (S_{\lambda_x} + K_{\lambda_x})/S_{\lambda_x}$ [34,36]. Furthermore, expressions for the backward and forward scattering coefficients for collimated light, respectively, denoted by S_{1,λ_x} and S_{2,λ_x}, have been reported in the literature [34]. Expressions for K_{λ_x}, S_{λ_x}, S_{1,λ_x}, and S_{2,λ_x} will be discussed later.

The unattenuated collimated flux that was neither absorbed nor scattered at depth z follows the Beer–Lambert law and is expressed as [27]

$$F_{c,\lambda_x}(z) = (1 - \rho_{01}) F_{0,\lambda_x} e^{-K_{c,\lambda_x} z}, \quad (9)$$

where F_{0,λ_x} is the incident collimated flux and K_{c,λ_x} is the effective extinction coefficient for the collimated flux at the excitation wavelength λ_x. The specular reflectivity for normally incident radiation, denoted by ρ_{01}, is given by [27]

$$\rho_{01} = \left(\frac{n_1 - n_0}{n_1 + n_0}\right)^2, \quad (10)$$

where n_1 and n_0 are the refractive indices of the medium and surrounding air, respectively. The boundary condition for the diffuse fluxes in the positive direction $F^+_{\lambda_x}(0)$ can be expressed as [34]

$$F^+_{\lambda_x}(0) = \rho_{10} F^-_{\lambda_x}(0), \quad (11)$$

where the hemispherical–hemispherical reflectivity ρ_{10} is the fraction of diffuse flux radiating from within the medium reflected back into the medium due to index mismatch and given by [37]

$$\rho_{10} = \int_0^{\pi/2} \rho''(\theta_i) \sin 2\theta_i \mathrm{d}\theta_i. \quad (12)$$

The directional specular reflectivity of the interface for the angle of incidence θ_i is denoted by $\rho''(\theta_i)$ and expressed as [27]

$$\rho_{//}(\theta_i) = \begin{cases} \frac{1}{2}\left[\frac{\sin^2(\theta_i-\theta_t)}{\sin^2(\theta_i+\theta_t)} + \frac{\tan^2(\theta_i-\theta_t)}{\tan^2(\theta_i+\theta_t)}\right] & \text{for } \theta_i \le \theta_c \\ 1 & \text{for } \theta_i > \theta_c \end{cases}. \quad (13)$$

The angle of transmittance θ_t is determined by Snell's law (i.e., $n_0 \sin\theta_t = n_1 \sin\theta_i$), and θ_c is the critical angle defined as $\theta_c = \sin^{-1}(n_0/n_1)$ [27]. Since the negative flux $F^-_{\lambda_x}(z)$ vanishes as z goes to infinity, the following boundary condition is imposed [34]:

$$F^-_{\lambda_x}(z \to \infty) = 0. \quad (14)$$

By solving Eqs. (6) and (7) and evaluating the integral in Eq. (3), $G_{\lambda_x}(z)$ can be expressed as [34]

$$\begin{aligned} G_{\lambda_x}(z) &= 2\pi[F^+_{\lambda_x}(z) + F^-_{\lambda_x}(z) + F_{c,\lambda_x}(z)] \\ &= (1-\rho_{01})F_{0,\lambda_x}(k_1 e^{-b_{\lambda_x}S_{\lambda_x}z} + k_2 e^{-K_{c,\lambda_x}z}), \end{aligned} \quad (15)$$

where $b_{\lambda_x} = \sqrt{a^2_{\lambda_x} - 1}$ [36]. Expressions for k_1 and k_2 can be determined from the boundary conditions given by Eqs. (11) and (14) as [34]

$$k_1 = \frac{2\pi(a_{\lambda_x} - b_{\lambda_x} + 1)\{K_{c,\lambda_x}(\rho_{10}S_{1,\lambda_x} + S_{2,\lambda_x}) + S_{\lambda_x}[(a_{\lambda_x}\rho_{10} - 1)S_{1,\lambda_x} + (\rho_{10} - a_{\lambda_x})S_{2,\lambda_x}]\}}{((a_{\lambda_x} + b_{\lambda_x})\rho_{10} - 1)(K^2_{c,\lambda_x} - b^2_{\lambda_x}S^2_{\lambda_x})}, \quad (16)$$

$$k_2 = \frac{2\pi\{K^2_{c,\lambda_x} + (S_{2,\lambda_x} - S_{1,\lambda_x})K_{c,\lambda_x} - S_{\lambda_x}[S_{\lambda_x}b^2_{\lambda_x} + (a_{\lambda_x} + 1)(S_{1,\lambda_x} + S_{2,\lambda_x})]\}}{K^2_{c,\lambda_x} - b^2_{\lambda_x}S^2_{\lambda_x}}. \quad (17)$$

Unlike k_1, which depends on n_1 through ρ_{10} given by Eq. (12), k_2 is independent of n_1.

C. Two-Flux Approximation of Fluorescence Light Transport

Fluorescence light transport can be similarly approximated by two fluxes in the positive and negative z directions, respectively, as illustrated in Fig. 1(b). In this case, Eq. (2) reduces to the following two coupled ordinary differential equations [8,15]:

$$\frac{dF^+_{\lambda_f}}{dz} = -a_{\lambda_f}S_{\lambda_f}F^+_{\lambda_f} + S_{\lambda_f}F^-_{\lambda_f} + \frac{1}{2}\gamma_{xf}(z)G_{\lambda_x}(z), \quad (18)$$

$$\frac{dF^-_{\lambda_f}}{dz} = -S_{\lambda_f}F^+_{\lambda_f} + a_{\lambda_f}S_{\lambda_f}F^-_{\lambda_f} - \frac{1}{2}\gamma_{xf}(z)G_{\lambda_x}(z), \quad (19)$$

where $F^+_{\lambda_f}$ and $F^-_{\lambda_f}$ represent the diffuse fluxes at the fluorescence wavelength λ_f propagating in the positive and negative z directions, respectively. Equations (18) and (19) are coupled to Eqs. (6) and (7) through the isotropic fluorescence emission source term $\gamma_{xf}(z)G_{\lambda_x}(z)$. Finally, boundary conditions for Eqs. (18) and (19) can be stated as [34]

$$F^+_{\lambda_f}(0) = \rho_{10}F^-_{\lambda_f}(0), \quad F^-_{\lambda_f}(z \to \infty) = 0. \quad (20)$$

Various solutions of Eqs. (18) and (19) have been proposed to approximate the fluorescence signal from slabs of finite thickness [8,15,38,39] or semi-infinite homogeneous layers [16]. Kokhanovsky [38] derived expressions for the excitation and fluorescence fluence rates based on the two-flux approximation for homogeneous slabs and semi-infinite media exposed to diffuse incident irradiation. Furthermore, the author provided relationships between the radiative characteristics of strongly scattering slabs and the two-flux approximation parameters. However, this model assumed the refractive index of the medium and its surroundings to be identical and equal to 1.0. Furthermore, the author did not compare the accuracy of the two-flux approximation with a more accurate solution of the radiative transfer equation and instead suggested that the expressions derived were "only approximately valid" [38]. Similarly, Ramos and Lagorio [8], Shakespeare and Shakespeare [15], and Durkin *et al.* [16] used the conventional two-flux approximation [35] to analyze fluorescence emission from turbid slabs and semi-infinite media irradiated by diffusely incident light. In each case, the medium was assumed to be homogeneous, to contain a single fluorophore, and to exhibit no index mismatch with the surrounding. Unlike Kokhanovsky [38], these studies also presented inverse methods for determining the intrinsic fluorescence coefficient of media from observed surface fluorescence and reflectance. These models were able to predict the shape of the intrinsic fluorescence spectrum of plant life [8], textiles [15], and human tissue [16] but could not be used to estimate its absolute value. Furthermore, none of these models could be used to analyze fluorescence from multilayer media exposed to normal incident and

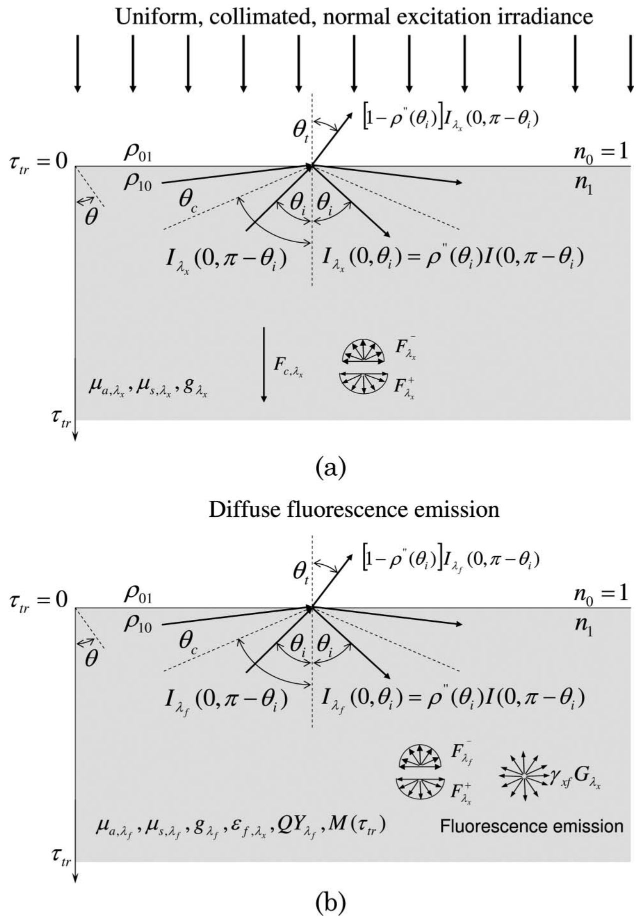

Fig. 1. Schematic of the geometry considered along with coordinate system, boundary conditions, and optical properties for the (a) excitation wavelength λ_x and (b) fluorescence emission wavelength λ_f.

collimated excitation light featuring index mismatched with the surroundings and/or that exhibited depth-dependent fluorophore concentration.

The current study extends the two-flux approximation to absorbing, scattering, and fluorescing multilayer media. It extends the two-flux approximation to accurately model (i) the local excitation fluence rate in semi-infinite media and (ii) the fluorescence emission from media in which fluorophore concentration varies stepwise with depth. Additionally, here the illumination considered was collimated and normally incident as opposed to diffuse. Furthermore, a single semiempirical parameter was fitted to match our model predictions for the excitation fluence rate and fluorescence emission with results from Monte Carlo simulations.

D. Two-Flux Approximation Coefficients

For strongly forward scattering media, the relationship between the effective absorption coefficient for collimated light $K_{c,\lambda}$ appearing in Eq. (9) and $\mu_{a,\lambda}$, $\mu_{s,\lambda}$, and g_λ can be expressed as [34,40,41]

$$K_{c,\lambda} = \mu_{a,\lambda} + (1 - g_\lambda^2)\mu_{s,\lambda}. \tag{21}$$

Furthermore, the coefficients K_λ and S_λ are proportional to $\mu_{a,\lambda}$ and $\mu_{s,\lambda}$, according to [36,42]

$$\mu_{a,\lambda} = \eta_\lambda K_\lambda, \quad \mu_{s,\lambda}(1 - g_\lambda) = \chi_\lambda S_\lambda, \tag{22}$$

where η_λ and χ_λ are expressed as [36]

$$\eta_\lambda = (\phi_\lambda - 1)(1 - \omega_{tr,\lambda})/\zeta_{d,\lambda}(\phi_\lambda + 1),$$
$$\chi_\lambda = -\omega_{tr,\lambda}(\phi_\lambda - \phi_\lambda^{-1})/(2\zeta_{d,\lambda}). \tag{23}$$

The function ϕ_λ is defined as [33]

$$\phi_\lambda = \frac{\zeta_{d,\lambda} + \ln(1 - \zeta_{d,\lambda})}{\zeta_{d,\lambda} - \ln(1 + \zeta_{d,\lambda})}, \tag{24}$$

where $\zeta_{d,\lambda}$ is the root of the characteristic equation [33]

$$\omega_{tr,\lambda} = \frac{2\zeta_{d,\lambda}}{\ln[(1 + \zeta_{d,\lambda})/(1 - \zeta_{d,\lambda})]}. \tag{25}$$

An approximate expression for $\zeta_{d,\lambda}^2$ as a function of $\omega_{tr,\lambda}$ was found to be [42]

$$\zeta_{d,\lambda}^2 = \frac{47}{52} + \frac{31}{49}\omega_{tr,\lambda} - \frac{49}{54}\omega_{tr,\lambda}^2 - \frac{17}{27}\omega_{tr,\lambda}^3. \tag{26}$$

The relative difference between Eq. (26) and the exact solution of Eq. (25) was determined to be less than 1% for $0.40 < \omega_{tr} < 1.00$ [42].

3. Methods

A. Model Assumptions and Geometry

In this study, biological tissue was approximated as a semi-infinite, one-dimensional, strongly scattering medium. It was characterized by the properties μ_{a,λ_x}, μ_{s,λ_x}, g_{λ_x}, and n_1 at the excitation wavelength λ_x. The incident light source was modeled as a collimated, monochromatic, normally incident beam of infinite radius and intensity $I_{\lambda_x}(0,\theta) = F_{0,\lambda_x}\delta(\theta)$. All the interfaces were considered smooth and optically flat.

In practice, tissue excitation is typically performed with light between 260 and 500 nm, while fluorescence emission is measured between 350 and 700 nm [1,7]. The ranges for optical properties considered in this study were chosen to include those of human dermis in this wavelength range. Then, the asymmetry factor g_λ varies between 0.70 and 0.90 [43]. Furthermore, Fig. 2(a) shows the transport single scattering albedo of the human dermis as a function of wavelength between 300 and 700 nm measured *in vitro* as reported in the literature [43–45]. Optical characteristics of the dermis below 300 nm were not available. While there is disagreement between the values reported in various studies, the single scattering albedo is typically greater than 0.80. Furthermore, tissue fluorescence emission for one-dimensional, homogeneous, semi-infinite media has been shown to depend on ω_{tr,λ_x} and ω_{tr,λ_f} as well as on the transport

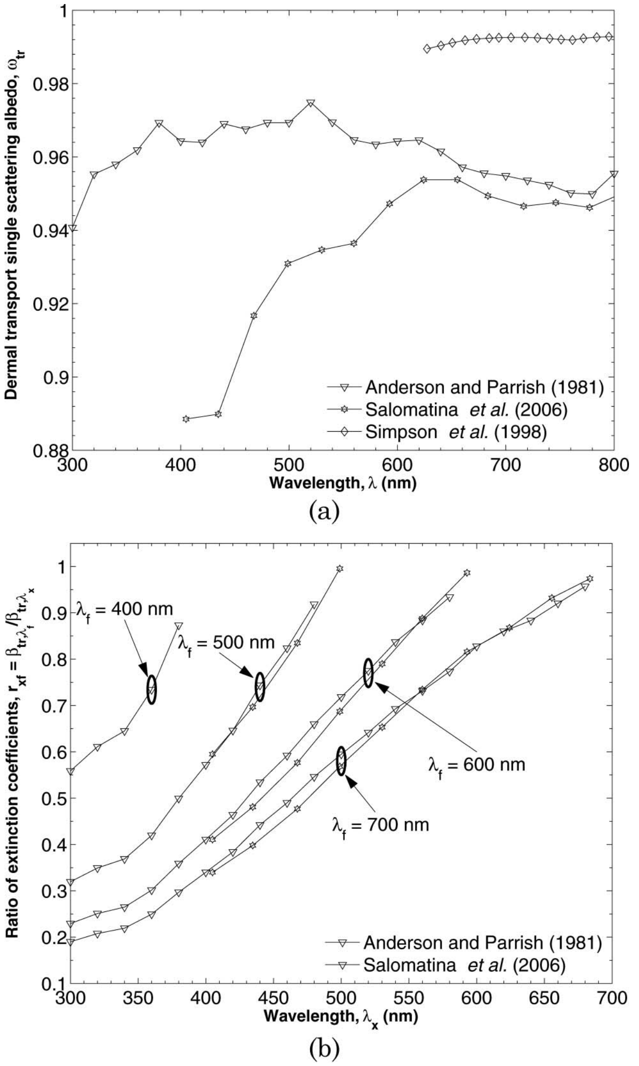

Fig. 2. (a) Transport single scattering albedo as a function of wavelength for human dermis [43–45]. (b) Ratio of extinction coefficients r_{xf} as a function of excitation wavelength λ_x and emission wavelength λ_f equal to 400, 500, 600, and 700 nm for the human dermis [43,44].

extinction coefficient ratio $r_{xf} = \beta_{tr,\lambda_f}/\beta_{tr,\lambda_x}$, and not on the individual values of β_{tr,λ_f} and β_{tr,λ_x} [11,19]. Figure 2(b) shows r_{xf} as a function of λ_x between 300 and 700 nm for λ_f equal to 400, 500, 600, and 700 nm for the human dermis. It indicates that r_{xf} ranges between 0.2 and 1.0 in this wavelength range. Thus, to simulate human dermis and a wide range of other biological tissues such as muscles, colon, or brain [29], we considered cases when ω_{tr,λ_x} ranged between 0.50 and 0.99, g_{λ_x} between 0.70 and 0.90, and n_1 between 1.00 and 2.00.

Furthermore, it was assumed that μ_{a,λ_f}, μ_{s,λ_f}, and g_{λ_f} at the emission wavelength λ_f were independent of location. Then, ω_{tr,λ_f} was assumed to vary between 0.50 and 0.99, g_{λ_f} between 0.70 and 0.90, and r_{xf} between 0.20 and 5. However, the intrinsic fluorescence coefficient γ_{xf} was assumed to vary with the optical thickness defined as $\tau_{tr,\lambda_x} = \beta_{tr,\lambda_x} z$. The intrinsic fluorescence coefficient was given by

$$\gamma_{xf}(\tau_{tr,\lambda_x}) = \epsilon_{f,\lambda_x} \mathrm{QY}_{xf}(\tau_{tr,\lambda_x}) M(\tau_{tr,\lambda_x}). \tag{27}$$

Figure 3 shows the three different fluorophore concentration profiles $M(\tau_{tr,\lambda_x})$ considered in this study. Light regions represent the medium where $M(\tau_{tr,\lambda_x}) = 0\,\mathrm{mole/cm^3}$, while dark regions represent regions where $M(\tau_{tr,\lambda_x})$ is constant and strictly positive. Figure 3(a) corresponds to a two-layer medium where the fluorophore is uniformly distributed in the medium for $\tau_{tr,\lambda_x} > \tau_{tr,\lambda_x,1}$ below a nonfluorescing layer. In this case, $M^S(\tau_{tr,\lambda_x}) = Au(\tau_{tr,\lambda_x} - \tau_{tr,\lambda_x,1})$, where A is an arbitrary constant and $u(\tau_{tr,\lambda_x} - \tau_{tr,\lambda_x,1})$ is the step function defined by

$$u(\tau_{tr,\lambda_x} - \tau_{tr,\lambda_x,1}) = \begin{cases} 1 & \text{if } \tau_{tr,\lambda_x} \geq \tau_{tr,\lambda_x,1} \\ 0 & \text{if } \tau_{tr,\lambda_x} < \tau_{tr,\lambda_x,1} \end{cases}. \tag{28}$$

Figure 3(b) depicts the concentration profile $M^H(\tau_{tr,\lambda_x}) = Au(\tau_{tr,\lambda_x})$ corresponding to a homogeneous fluorophore distribution. Finally, Fig. 3(c) depicts the concentration profile $M^L(\tau_{tr,\lambda_x,1}, \tau_{tr,\lambda_x,2}) = A[u(\tau_{tr,\lambda_x} - \tau_{tr,\lambda_x,1}) - u(\tau_{tr,\lambda_x} - \tau_{tr,\lambda_x,2})]$ corresponding to a three-layer system, where the fluorophore is uniformly distributed in the layer between depths $\tau_{tr,\lambda_x,1}$ and $\tau_{tr,\lambda_x,2}$ and surrounded by two nonfluorescing layers.

B. Monte Carlo Simulations

The RTE for excitation light given by Eq. (1) was solved using the Monte Carlo simulation software developed by Wang and Jacques [46,47] for light transfer through nonemitting, absorbing, and scattering media. This software was modified according to Welch *et al.* [6] to solve the RTE for fluorescence emission in the medium given by Eq. (2). The Henyey–Greenstein scattering phase function given

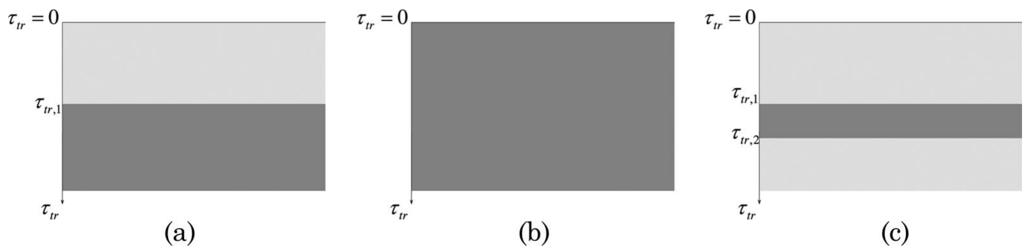

Fig. 3. Schematic of (a) step, (b) homogeneous, and (c) layered fluorophore concentration profiles $M^S(\tau_{tr,\lambda_x})$, $M^H(\tau_{tr,\lambda_x})$, and $M^L(\tau_{tr,\lambda_x})$, respectively. Light gray represents the medium without fluorophore [$M(\tau_{tr,\lambda_x}) = 0\,\mathrm{mole/cm^3}$], while dark gray represents regions with fluorophore [$M(\tau_{tr,\lambda_x}) = A\,\mathrm{mole/cm^3}$].

by Eq. (4) was used to account for anisotropic scattering. The variance in the prediction of fluorescence intensity emerging at the surface of the medium increased as the transport single scattering albedo ω_{tr,λ_f} decreased, because absorption by the medium dominated over scattering resulting in fewer backscattered fluorescence photons. Thus, the number of simulated photon packets per simulation was increased until the variance associated with the fluorescence emission fell below 1% for the most stringent case of a semi-infinite homogeneous medium with $\omega_{tr,\lambda_f} = 0.50$. The variance for the most stringent case was calculated from ten repetitions of the same simulation. Each simulation required 100,000 photon packets or less to achieve the convergence criteria.

4. Analysis

A. Semiempirical Model of Excitation Fluence

The solution to Eqs. (6) and (7) given by Eqs. (15)–(17) has been shown to give poor estimates of the excitation fluence rate $G_{\lambda_x}(z)$ for media with index mismatch at the media–air boundary or when the semi-infinite medium is weakly scattering and the excitation source is collimated [17,48]. In the current study, the coefficients k_1 and k_2 in Eq. (15) were determined by fitting the local fluence rate $G_{\lambda_x}(z)$ predicted by Eq. (15) to that obtained by Monte Carlo simulations. By rearranging Eqs. (22)–(25), the product $b_{\lambda_x} S_{\lambda_x} z$ in the first term of Eq. (15) can be rewritten as $\zeta_{d,\lambda_x}\beta_{tr,\lambda_x} z = \zeta_{d,\lambda_x}\tau_{tr,\lambda_x}$ [36,42]. Furthermore, by taking a polynomial Taylor series expansion of K_{c,λ_x} defined by Eq. (21) with respect to g_{λ_x} about $g_{\lambda_x} = 1$, the coefficient K_{c,λ_x} can be expressed approximately as a function of β_{tr,λ_x}:

$$K_{c,\lambda_x} \approx \mu_{a,\lambda_x} + 2(1 - g_{\lambda_x})\mu_{s,\lambda_x} = \beta_{tr,\lambda_x}(1 + \omega_{tr,\lambda_x}). \quad (29)$$

Then, by introducing the coefficient $\zeta_{c,\lambda_x} = (1 + \omega_{tr,\lambda_x})$, Eq. (15) can be rewritten exclusively as a function of τ_{tr,λ_x}:

$$G_{\lambda_x}(\tau_{tr,\lambda_x}) = (1 - \rho_{01})F_{0,\lambda_x}(k_1 e^{-\zeta_{d,\lambda_x}\tau_{tr,\lambda_x}} + k_2 e^{-\zeta_{c,\lambda_x}\tau_{tr,\lambda_x}}). \quad (30)$$

Equation (30) can be further simplified by considering conservation of excitation energy. Indeed, the amount of excitation energy absorbed by the medium in a differential element dz is $\mu_{a,\lambda_x} G_{\lambda_x}(z) dz$ [27]. Thus, the sum of the energy absorbed and the total energy reflected by the medium must be equal to the incident excitation energy F_{0,λ_x}. This can be expressed as [27]

$$F_{0,\lambda_x} = \int_0^\infty \mu_{a,\lambda_x} G_{\lambda_x}(z)\mathrm{d}z + F_{0,\lambda_x}(R_{d,\lambda_x} + \rho_{01}), \quad (31)$$

where the integral term represents the excitation energy absorbed throughout the medium, and $F_{0,\lambda_x} R_{d,\lambda_x}$ and $F_{0,\lambda_x}\rho_{01}$ represent the energy diffusely and specularly reflected by the medium, respectively. The quantity $F_{0,\lambda_x}(R_{d,\lambda_x} + \rho_{01})$ can be measured experimentally or calculated analytically [27,42]. By substituting Eq. (30) into Eq. (31), k_1 can be expressed as

$$k_1 = \zeta_{d,\lambda_x}\left(\frac{1 - R_{d,\lambda_x} - \rho_{01}}{1 - \omega_{tr,\lambda_x}} - \frac{k_2}{1 + \omega_{tr,\lambda_x}}\right). \quad (32)$$

Therefore, calculating $G_{\lambda_x}(\tau_{tr,\lambda_x})$ given by Eq. (15) for any value of ω_{tr,λ_x}, β_{tr,λ_x}, and n_1 required the knowledge of a single empirical fitting parameter, namely, k_2.

B. Fluorescence Emission

In this section, an expression for the fluorescence flux emerging from the tissue and given by $(1 - \rho_{01}) F^-_{\lambda_f}(0)$ is developed. To do so, the local excitation fluence rate given by Eq. (30) is used to solve Eqs. (18) and (19) with various fluorophore concentration profiles to yield

$$(1 - \rho_{10})F^-_{\lambda_f}(0) = (1 - \rho_{10})F_{0,\lambda_x}\epsilon_{f,\lambda_x}\mathrm{QY}_{xf}\mathrm{A}T_{xf}. \quad (33)$$

The quantity T_{xf} is a dimensionless function and will be referred to as the transfer function.

Before considering the different fluorophore concentration profiles depicted in Fig. 3, Eqs. (18) and (19) were solved for an isotropic emission source of unit intensity at an arbitrary optical depth $\tau_{tr,0}$. This so-called impulse response was found by replacing $\gamma_{xf}(z)G_{\lambda_x}(z)$ with $\delta(z - z_0)$ in Eqs. (18) and (19). The corresponding impulse transfer function $T^\delta_{xf}(\tau_{tr,\lambda_x,0})$ can be expressed as

$$T^\delta_{xf}(\tau_{tr,\lambda_x,0}) = \frac{(1 - \rho_{10})(a_{\lambda_f} + b_{\lambda_f} + 1)e^{-\zeta_{d,\lambda_f} r_{xf}\tau_{tr,\lambda_x,0}}}{2(a_{\lambda_f} + b_{\lambda_f} - \rho_{10})}. \quad (34)$$

Then, for any arbitrary concentration profile $M(\tau_{tr,\lambda_x})$, the fluorescence emission transfer function is given by

$$T_{xf} = \frac{1}{\beta_{tr,\lambda_x}}\int_0^\infty M(\tau_{tr,\lambda_x})G_{\lambda_x}(\tau_{tr,\lambda_x})T^\delta_{xf}(\tau_{tr,\lambda_x})\mathrm{d}\tau_{tr,\lambda_x}. \quad (35)$$

Evaluating Eq. (35) for the two-layer concentration profile $M^S(\tau_{tr,\lambda_x}) = Au(\tau_{tr,\lambda_x} - \tau_{tr,\lambda_x,1})$ [Fig. 3(a)] yields

$$T^S_{xf}(\tau_{tr,\lambda_x,1}) = \left(\frac{k_1 e^{-(\zeta_{d,\lambda_f} r_{xf} + \zeta_{d,\lambda_x})\tau_{tr,\lambda_x,1}}}{\zeta_{d,\lambda_f} r_{xf} + \zeta_{d,\lambda_x}} + \frac{k_2 e^{-(\zeta_{d,\lambda_f} r_{xf} + \zeta_{c,\lambda_x})\tau_{tr,\lambda_x,1}}}{\zeta_{d,\lambda_f} r_{xf} + \zeta_{c,\lambda_x}}\right)\frac{T^\delta_{xf}(0)}{\beta_{tr,\lambda_x}}. \quad (36)$$

Moreover, the transfer function for a homogeneous medium T^H_{xf} [Fig. 3(b)] can be determined by setting

$\tau_{tr,\lambda_x,1}$ to zero in Eq. (36):

$$T_{xf}^H = T_{xf}^S(0) = \left(\frac{k_1}{\zeta_{d,\lambda_f} r_{xf} + \zeta_{d,\lambda_x}} + \frac{k_2}{\zeta_{d,\lambda_f} r_{xf} + \zeta_{c,\lambda_x}}\right) \frac{T_{xf}^\delta(0)}{\beta_{tr,\lambda_x}}. \quad (37)$$

Finally, the transfer function due to the three-layer concentration profile depicted in Fig. 3(c) and given by $M^L(\tau_{tr,\lambda_x,1}, \tau_{tr,\lambda_x,2}) = A[u(\tau_{tr,\lambda_x} - \tau_{tr,\lambda_x,1}) - u(\tau_{tr,\lambda_x} - \tau_{tr,\lambda_x,2})]$ can be expressed as

$$T_{xf}^L(\tau_{tr,\lambda_x,1}, \tau_{tr,\lambda_x,2}) = T_{xf}^S(\tau_{tr,\lambda_x,1}) - T_{xf}^S(\tau_{tr,\lambda_x,2}), \quad (38)$$

where $T_{xf}^S(\tau_{tr,\lambda_x})$ is defined by Eq. (36).

5. Results and Discussion

A. Local Excitation Fluence

Monte Carlo simulations were performed to calculate the normalized excitation fluence rate $G_{\lambda_x}(\tau_{tr,\lambda_x})/F_{0,\lambda_x}$ for ten values of ω_{tr,λ_x} between 0.50 and 0.99 and four values of n_1 between 1.00 and 2.00. The function $G_{\lambda_x}(\tau_{tr,\lambda_x})/F_{0,\lambda_x}$ was observed to be self-similar with respect to β_{tr,λ_x}, so β_{tr,λ_x} was set to unity for each simulation. A semi-infinite medium was simulated with a finite numerical grid of length L_{grid} in the z-direction set to be ten times the penetration depth for collimated light derived from diffusion theory so that $L_{\mathrm{grid}} = 10(3\mu_{a,\lambda_x}\beta_{tr,\lambda_x})^{-1/2}$ [40]. For this grid length, the finite slab was effectively semi-infinite, since all the energy of the collimated beam reaching $z = L_{\mathrm{grid}}$ vanished, thus satisfying the boundary condition given by Eq. (14). The grid consisted of N_z elements of length $\Delta z = L_{\mathrm{grid}}/N_z$. The number of grid elements N_z was set to be 200 as a compromise (i) to make Δz sufficiently small so as to capture the effects of internal reflectance on $G_{\lambda_x}(z)$ near the medium's surface and (ii) to ensure that the variance associated with the local fluence rate obtained by Monte Carlo simulations in each grid element was less than 1%.

The values of parameters k_1 and k_2 necessary in Eq. (30) were determined by minimizing the cost function (CF) defined as

$$\mathrm{CF} = \sqrt{\frac{1}{N_z}\sum_{i=1}^{N_z}[G_{\lambda_x}^{\mathrm{MC}}(i\Delta z) - G_{\lambda_x}(i\Delta z)]^2}, \quad (39)$$

corresponding to the root-mean-square error between the estimate of the excitation fluence rate predicted by Monte Carlo simulations $G_{\lambda_x}^{\mathrm{MC}}(z)$ and $G_{\lambda_x}(z)$ predicted by Eq. (30). Figure 4 shows k_1 and k_2 found by minimizing the CF as functions of the diffuse reflectance R_{d,λ_x} for n_1 equal to 1.33, 1.44, 1.77, and 2.00 and ω_{tr,λ_x} ranging between 0.50 and 0.99. These quantities were plotted as functions of R_{d,λ_x} in order to provide a simple relationship between the diffuse reflectance R_{d,λ_x}, which can be measured experimentally, and the local excitation fluence rate,

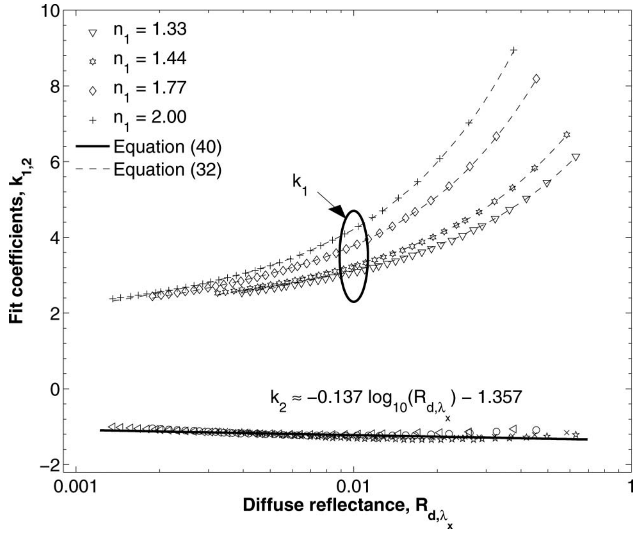

Fig. 4. Fitting parameters k_1 and k_2 retrieved using Monte Carlo simulations as a function of R_{d,λ_x} along with predictions by Eqs. (32) and (40) for n_1 between 1.33 and 2.00.

which cannot. The value of k_1 increased with increasing R_{d,λ_x} and n_1, while the value of k_2 decreased with increasing R_{d,λ_x} and was approximately invariant with n_1. In fact, regardless of the value of n_1, k_2 could be approximated by a linear relationship with the logarithm of R_{d,λ_x}, namely,

$$k_2 \approx -0.137\log_{10}(R_{d,\lambda_x}) - 1.357. \quad (40)$$

Values of k_1 computed from Eqs. (32) and (40) and those obtained by minimizing the CF agreed with each other to within 0.1%. In addition, the independence of k_2 with respect to n_1 was suggested by Eq. (17) by virtue of the fact that k_2 is independent of ρ_{10}. Note that Gardner *et al.* [12] used a similar approach by fitting six semiempirical parameters expressed as a function of the diffuse reflectance R_{d,λ_x}. The authors considered a semi-infinite and homogeneous medium with $n_1 = 1.33$ or 1.38, g ranging from 0.7 and 0.9, and ω_{tr} between 0 and 1.0. In contrast, Eqs. (30) and (32) predict the excitation fluence rate for (i) any values of n_1 between 1.0 and 2.0, (ii) g ranging from 0.7 and 0.9, and (iii) ω_{tr} between 0.5 and 0.99. The model depends on a single semiempirical parameter k_2 depending on only the diffuse reflectance, and it ensures energy conservation.

For illustration purposes, Fig. 5(a) shows the normalized excitation fluence rate $G_{\lambda_x}/F_{0,\lambda_x}$ calculated by Monte Carlo simulations and predicted by Eqs. (30), (32), and (40) as a function of $\zeta_{d,\lambda_x}\tau_{tr,\lambda_x}$ for ω_{tr,λ_x} between 0.50 and 0.99 and $n_1 = 1.44$. The index of refraction n_1 was chosen to be 1.44 to represent the human dermis in the visible range [29]. In practice, the index of refraction of the medium under investigation would need to be determined separately. Furthermore, tissue is typically excited at a wavelength where absorption is strong. Thus, the transport single scattering albedo at the excitation wavelength ω_{tr,λ_x} was chosen to be 0.700. We also showed the cases when the transport single scattering albedo at the emission wavelength ω_{tr,λ_f} is close to and much larger than that at the excitation wavelength ω_{tr,λ_x}.

The relative deviation between the model predictions and the Monte Carlo simulation was less than 5% for all values of $\zeta_{d,\lambda_x}\tau_{tr,\lambda_x}$ and for $\omega_{tr,\lambda_x} > 0.90$ typical of biological tissues [29]. For $\omega_{tr,\lambda_x} \leq 0.90$ and $\zeta_{d,\lambda_x}\tau_{tr,\lambda_x} < 1$, the model predictions of $G_{\lambda_x}(\tau_{tr,\lambda_x})$ deviated from Monte Carlo simulations by approximately 5%. For larger values of $\zeta_{d,\lambda_x}\tau_{tr,\lambda_x}$, model predictions and Monte Carlo simulations fell to within 1% of each other for all ω_{tr,λ_x}. Figure 5(b) shows the CF for n_1 between 1.33 and 2.00 and ω_{tr,λ_x} between 0.50 and 0.99. The absolute root-mean-square error was less than 4% for all values of n_1 and ω_{tr,λ_x} considered.

B. Fluorescence Emission from One- and Two-Layer Media

Figures 6(a) and 6(b) show T^S_{xf} estimated from a Monte Carlo simulation as a function of the transport optical thickness of the nonfluorescing layer $\tau_{tr,\lambda_x,1}$ associated with concentration profile $M^S(\tau_{tr,\lambda_x,1})$ for ω_{tr,λ_x} equal to 0.70, r_{xf} varying between 0.20 and 5.00, for ω_{tr,λ_f} equal to 0.750 and 0.900, respectively, and $n_1 = 1.44$. These values are representative of biological tissues [29]. Predictions by Eqs. (32), (36), and (40) are also plotted for comparison. Figure 6 indicates that T^S_{xf} decreased with increasing $\tau_{tr,\lambda_x,1}$. This can be attributed to the fact that the thickness of the top nonfluorescing layer increased. Thus, the fluorescence emission took place deeper inside the medium,

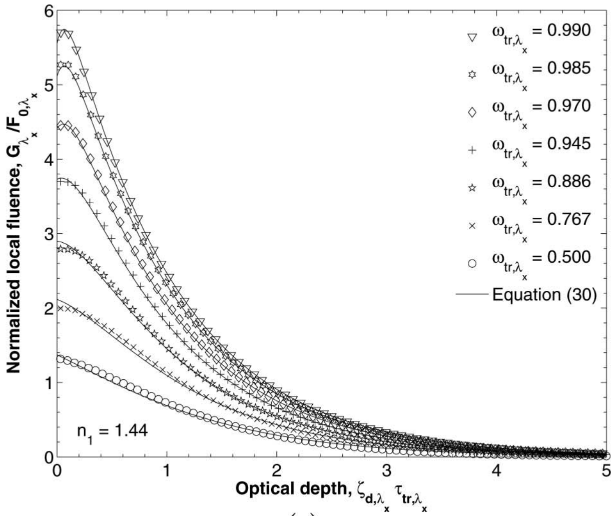

(a)

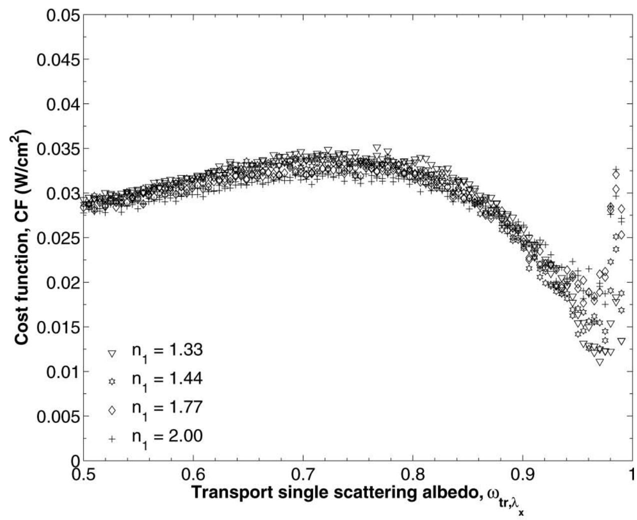

(b)

Fig. 5. (a) Normalized local excitation fluence rate as a function of the optical depth $\zeta_{d,\lambda_x}\tau_{tr,\lambda_x}$ predicted by Monte Carlo simulations and Eq. (30) for ω_{tr,λ_x} between 0.50 and 0.99 and $n_1 = 1.44$. (b) Root-mean-square (CF) [Eq. (39)] error as a function of the transport single scattering albedo ω_{tr,λ_x} between 0.50 and 0.99 and n_1 between 1.33 and 2.00.

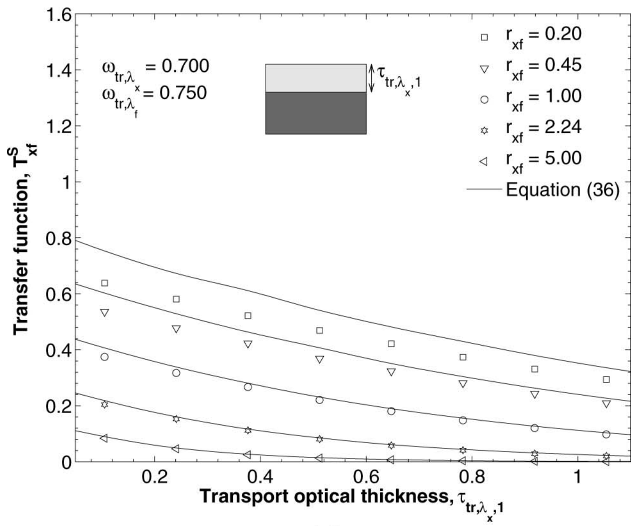

(a)

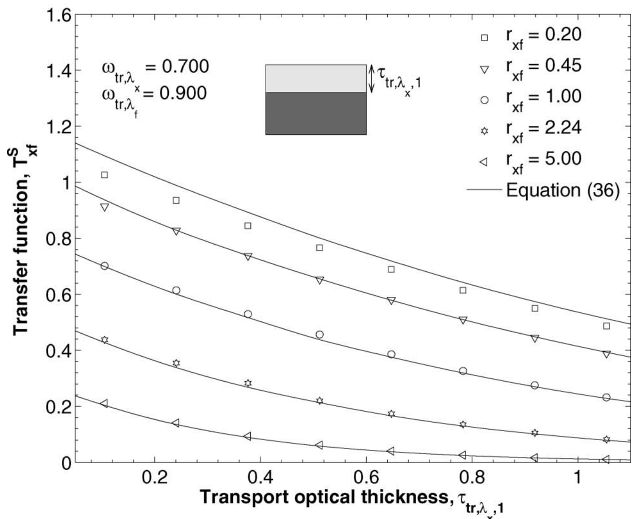

(b)

Fig. 6. Transfer function T^S_{xf} for step concentration profile $M^S(\tau_{tr,\lambda_x,1})$ versus the optical depth calculated by Monte Carlo simulations and predicted by Eq. (36) for $A = 1\,\text{mole/cm}^2$, $\omega_{tr,\lambda_x} = 0.70$, $n = 1.44$, r_{xf} between 0.2 and 5.0, and ω_{tr,λ_f} equal to (a) 0.750 and (b) 0.900.

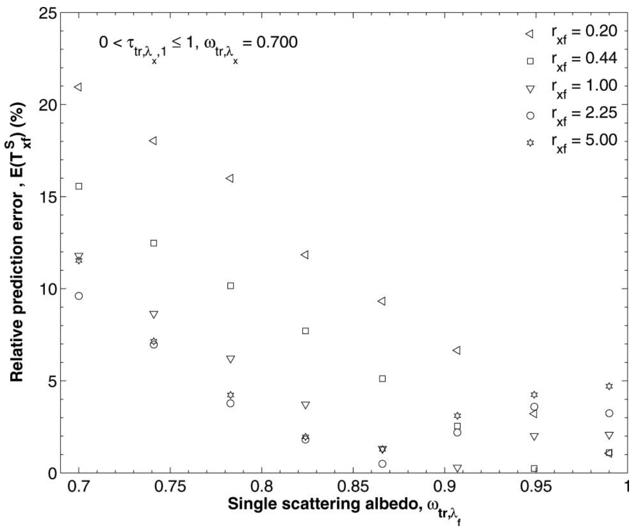

Fig. 7. Relative error between prediction of T^S_{xf} by Monte Carlo simulations and predicted by Eq. (36) averaged over $\tau_{tr,\lambda_x,1}$ between 0 and 1 for $A = 1\,\text{mole/cm}^2$, $\omega_{tr,\lambda_x} = 0.70$, $n = 1.44$, and r_{xf} between 0.20 and 5.00.

where the excitation fluence rate $G_{\lambda_x}(z)$ was reduced significantly. Additionally, the attenuation, or self-absorption [1], experienced by the fluorescent light as it traveled to the medium's surface was larger. Similarly, as the ratio of extinction coefficients $r_{xf} = \beta_{tr,\lambda_f}/\beta_{tr,\lambda_x}$ increased, T^S_{xf} decreased due to stronger attenuation by the medium at the fluorescent wavelength. For all cases considered, predictions by Eq. (36) followed the trend and magnitude of T^S_{xf}. In addition, prediction accuracy increased with increasing r_{xf} and ω_{tr,λ_f}. This is due to the fact that the accuracy of the two-flux approximation with the boundary condition given by Eq. (20) diminishes for optically thin media and improves for strongly scattering media [17]. For the sake of clarity, only results for $\omega_{tr,\lambda_x} =$

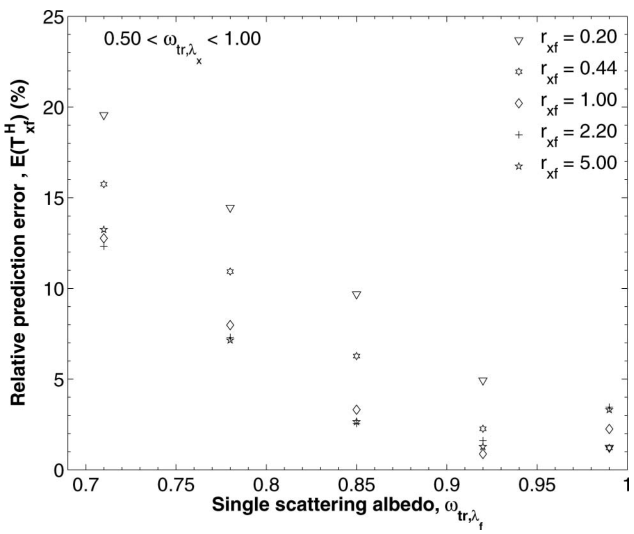

Fig. 8. Relative error between predictions of T^H_{xf} by Monte Carlo simulations and by Eq. (37) as a function of ω_{tr,λ_f} averaged over ω_{tr,λ_x} between 0.50 and 1.00 for r_{xf} between 0.20 and 5.00, $A = 1\,\text{mole/cm}^2$, and $n_1 = 1.44$.

0.70 were shown. However, Fig. 6 is representative of the accuracy of Eq. (36) in predicting T^S_{xf} for all the values of ω_{tr,λ_x} considered in this study.

In order to compare model predictions of T_{xf} used in Eq. (33) and Monte Carlo simulations for the fluorescence emission, the relative prediction error was defined as

$$E(T_{xf}) = \left|\frac{T_{xf} - T^{\text{MC}}_{xf}}{T^{\text{MC}}_{xf}}\right|, \tag{41}$$

where T^{MC}_{xf} is the transfer function predicted by Monte Carlo simulations. Figure 7 shows the relative prediction error $E(T^S_{xf})$ for concentration profile $M^S(\tau_{tr,\lambda_x,1})$ as a function of ω_{tr,λ_f} for ω_{tr,λ_x} equal to 0.700, r_{xf} between 0.20 and 5.00, and $\tau_{tr,1}$ between 0 and 1.0. The relative error T^S_{xf} was found to in-

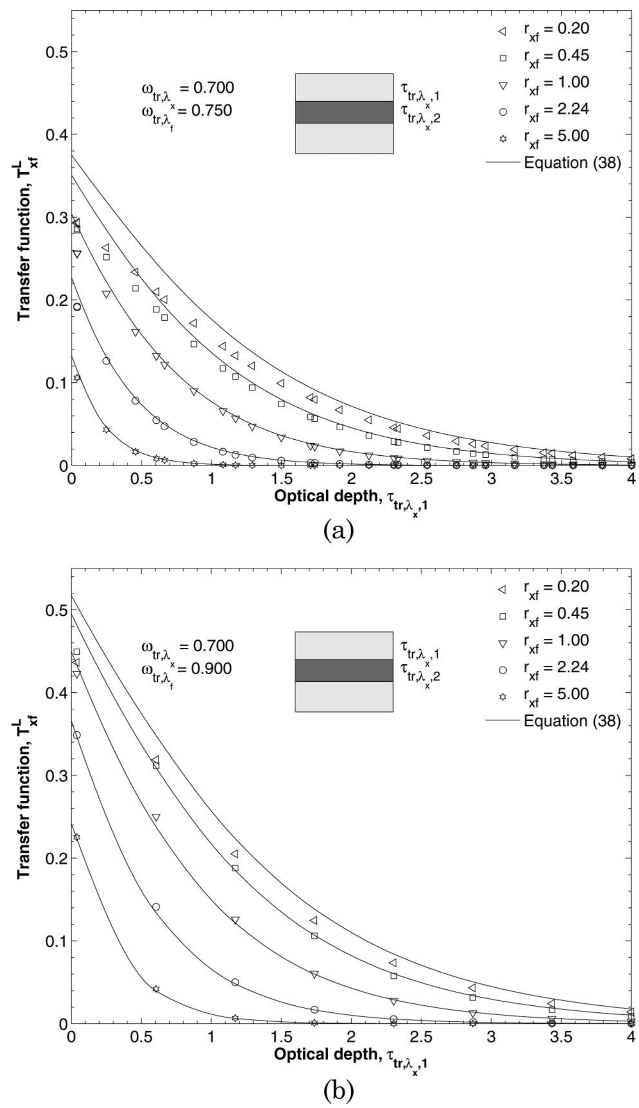

Fig. 9. Transfer function T^L_{xf} versus the optical depth predicted by Monte Carlo simulations and by Eq. (38) with $\omega_{tr,\lambda_x} = 0.700$, $A = 1\,\text{mole/cm}^2$, $n_1 = 1.44$, r_{xf} between 0.20 and 5.00, and $\tau_{tr,\lambda_x,2} - \tau_{tr,\lambda_x,1} = L\beta_{tr,\lambda_x}$ with $L = 1\,\text{cm}$ for ω_{tr,λ_f} equal to (a) 0.750 and (b) 0.900.

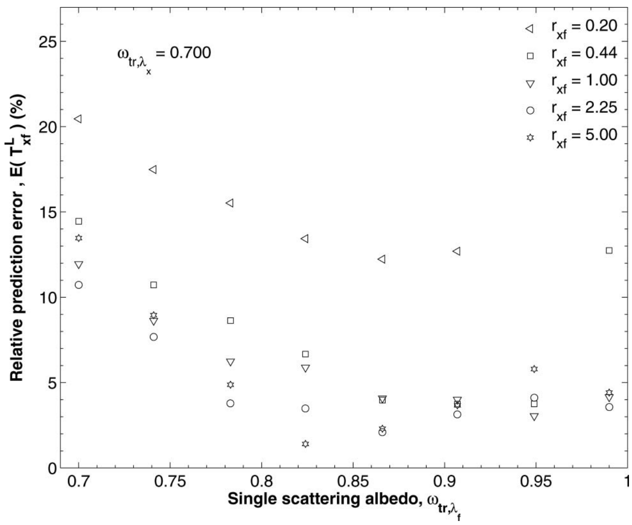

Fig. 10. Relative error between prediction of T^L_{xf} by Monte Carlo simulations and by Eq. (38) averaged over τ_{tr,λ_x} between 0 and 1 for $\omega_{tr,\lambda_x} = 0.70$, $A = 1\,\text{mole/cm}^2$, $n_1 = 1.44$, and r_{xf} between 0.20 and 5.00.

crease with decreasing ω_{tr,λ_f} and r_{xf} for the same reasons as those previously discussed. For example, it was less than 5% for $r_{xf} = 0.44$ and ω_{tr,λ_f} greater than 0.87. Furthermore, the relative error was less than 5% for all r_{xf} if ω_{tr,λ_f} was greater than 0.95.

Similar results were found for the concentration profile $M^H(\tau_{tr,\lambda_x})$ when $\tau_{tr,\lambda_x,1} = 0$. Figure 8 shows the relative prediction error $E(T^H_{xf})$ as a function of ω_{tr,λ_f} for ω_{tr,λ_x} between 0.5 and 1.0 and r_{xf} between 0.2 and 5.0. In this case, the relative error was less than 5% for all values of r_{xf} considered and for ω_{tr,λ_f} greater than 0.92. For ω_{tr,λ_f} less than 0.70, the relative prediction error was larger than 10%, so these values were not reported.

C. Fluorescence Emission from Three-Layer Media

Figures 9(a) and 9(b) show the transfer function T^L_{xf} estimated from Monte Carlo simulations as a function of the transport optical thickness of the top nonfluorescing layer $\tau_{tr,\lambda_x,1}$ for ω_{tr,λ_x} equal to 0.70, r_{xf} between 0.20 and 5.00, and for ω_{tr,λ_f} equal to 0.750 and 0.900, respectively. In each case, the thickness of the fluorescing layer was arbitrarily chosen such that $\tau_{tr,\lambda_x,2} - \tau_{tr,\lambda_x,1} = L\beta_{tr,\lambda_x}$ with $L = 0.1\,\text{cm}$. Predictions by Eq. (38) using Eqs. (32) and (40) are also plotted for comparison. As τ_{tr,λ_x} increased, the fluorescence emission occurred deeper within the medium, and thus, T^L_{xf} decreased, as was the case with T^S_{xf}.

Figure 10 shows the relative prediction error $E(T^L_{xf})$ as a function of ω_{tr,λ_f} for ω_{tr,λ_x} between 0.50 and 1.00, and r_{xf} between 0.20 and 5.00. Here, also, the relative error increased with decreasing ω_{tr,λ_f} and r_{xf}. For $r_{xf} = 0.44$, the prediction error was less than 5% for $\omega_{tr,f}$ greater than 0.87. Furthermore, the prediction error was typically less than 5% for all the values of r_{xf} greater than 0.44 and for ω_{tr,λ_f} greater than 0.97.

D. Model Limitations and Applicability

The current diffuse reflectance and fluorescence emission models are valid to semi-infinite media with optically smooth surfaces illuminated by uniform, collimated, and normally incident light and featuring uniform absorption and scattering coefficients and stepwise fluorophore concentration. They can be used to analyze reflectance measured by normal–normal optical probes, provided that a correction factor is determined to relate the normal–normal to the normal–hemispherical reflectance and fluorescence emission. The estimate of the fluorescence emission given by Eq. (33) is the integral of the emitted fluorescence intensity over the upper hemisphere. Similarly, the diffuse reflectance R_{d,λ_x} used in Eq. (31) is the integral of the diffusely reflected intensity over the upper hemisphere. These quantities can be measured in practice with an integrating sphere [1,29,30]. The current model can be used in an inverse method to retrieve the optical properties of tissues and the fluorophore concentration.

6. Conclusion

A model of excitation fluence rate and surface fluorescence emission from turbid media was developed for semi-infinite, absorption, and strongly forward scattering media. The model accounts for index mismatch between the medium (n_1 between 1.0 and 2.0) and the surrounding air ($n_0 = 1$). Using the two-flux approximation and invoking the energy conservation principle, the local excitation fluence rate was successfully modeled by Eqs. (30) and (32) with a single semi-empirical parameter, depending only on diffuse reflectance [Eq. (40)]. Then, the total surface fluorescence emission was simulated for (i) homogeneous semi-infinite media, (ii) media with a semi-infinite fluorescing layer underneath a nonfluorescing layer, and (iii) media with a discrete fluorescing layer embedded in a nonfluorescing semi-infinite layer. For ω_{tr,λ_f} greater than 0.90 and r_{xf} greater than 1, model predictions of the surface fluorescence emission were within 5% of results by Monte Carlo simulations for all values of ω_{tr,λ_x}, β_{tr,λ_x}, and n_1 considered. The current model can be used to quickly and accurately simulate the local fluence rate and surface fluorescence emission of biological media, such as the skin, or to analyze fluorescence spectroscopy data gathered from *in vivo* biological samples to recover intrinsic fluorescence spectra using an inverse method.

Nomenclature

A:	fluorophore concentration, mole/cm^3
a, b:	two-flux dimensionless parameters
CF:	cost function
F^+, F^-:	diffuse forward and backward fluxes, W/cm$^2\cdot$nm
F_0:	radiative flux of incident beam, W/cm$^2\cdot$nm
g:	Henyey–Greenstein asymmetry factor
G:	local fluence rate, W/cm$^2\cdot$nm
I:	radiation intensity, W/cm$^2\cdot$sr$\cdot$nm
$\hat{r}$:	position vector, cm
k_1, k_2:	fitting coefficients appearing in Eq. (15)

K: two-flux effective absorption coefficient for diffuse light, 1/cm
K_c: two-flux effective absorption coefficient for collimated light, 1/cm
$M(\tau_{tr,\lambda_x})$: fluorophore molar concentration profile, mole/cm^3
n_0, n_1: index of refraction of the air and medium
N_z: integer value appearing in Eq. (39)
r_{xf}: ratio of extinction coefficients, $\beta_{tr,\lambda_f}/\beta_{tr,\lambda_x}$
R: diffuse reflectance
$\hat{s}$: unit vector in a given direction
S: two-flux effective scattering coefficient for diffuse light, 1/cm
S_1, S_2: two-flux backward and forward scattering coefficients for collimated light, 1/cm
T: transfer function
QY: quantum yield
z: distance into the medium surface, cm
Δz: thickness of a single grid element used for Monte Carlo simulations, cm

Greek Symbols

β_{tr}: transport extinction coefficient, 1/cm
γ_{xf}: intrinsic fluorescence coefficient, 1/cm
ε_f: linear molar absorption coefficient of the fluorophore, cm^{-1}/(mole/cm^3)
ζ_d: root of characteristic Eq. (25)
ζ_c: linearized parameter defined by Eq. (29)
η, χ: parameters defined by Eq. (23)
θ: polar angle, rad
θ_i: angle of incidence on interface, rad
θ_t: exit angle defined in Fig. 1, rad
θ_c: critical angle for total internal reflection, rad
μ_a: linear absorption coefficient of the medium, cm^{-1}
μ_s: linear scattering coefficient, cm^{-1}
$\mu_{s,tr}$: transport scattering coefficient $[= \mu_s(\lambda)[1 - g(\lambda)]]$, cm^{-1}
ρ_{01}: specular reflectivity to normally incident light
ρ_{10}: hemispherical-hemispherical reflectivity
$\rho''(\theta_i)$: directional specular reflectivity
$\tau_{tr,\lambda_x,1}$: transport optical thickness
ϕ: parameter defined by Eq. (24)
Φ: scattering phase function, sr^{-1}
ω: single scattering albedo
ω_{tr}: transport single scattering albedo
Ω: solid angle, sr

Subscripts

λ_f: fluorescence emission wavelength
λ_x: excitation wavelength

Superscripts

δ: impulse concentration profile
S: step concentration profile
H: homogeneous concentration profile
L: three-layer concentration profile
MC: Monte Carlo simulations

The authors acknowledge the partial financial support of the Access Business Group in Ada, Michigan, and J. Leverett, P Seehra, and R. Roth for useful discussions.

References

1. M. A. Mycek and B. W. Pogue, *Handbook of Biomedical Fluorescence* (Marcel Dekker, 2003).
2. J. R. Lakowicz, *Principles of Fluorescence Spectroscopy* (Kluwer Academic, 1999).
3. N. Kollias, G. Zonios, and G. N. Stamatas, "Fluorescence spectroscopy of skin," Vib. Spectrosc. **28**, 17–23 (2002).
4. I. Georgakoudi, B. C. Jacobson, M. G. Müller, E. E. Sheets, K. Badizadegan, D. L. Carr-Locke, C. P. Crum, C. W. Boone, R. R. Dasari, and J. Van Dam, and M. S. Feld, "NAD(P)H and collagen as *in vivo* quantitative fluorescent biomarkers of epithelial precancerous changes," Cancer Res. **62**, 682–687 (2002).
5. I. Georgakoudi, B. C. Jacobson, J. Van Dam, V. Backman, M. B. Wallace, M. G. Müller, Q. Zhang, K. Badizadegan, D. Sun, and G. A. Thomas, L. T. Perelman, and M. S. Feld, "Fluorescence, reflectance, and light-scattering spectroscopy for evaluating dysplasia in patients with Barrett's esophagus," Gastroenterology **120**, 1620–1629 (2001).
6. A. J. Welch, C. Gardner, R. Richards-Kortum, E. Chan, G. Criswell, J. Pfefer, and S. Warren, "Propagation of fluorescent light," Lasers Surg. Med. **21**, 166–178 (1997).
7. K. M. Katika and L. Pilon, "Steady-state directional diffuse reflectance and fluorescence of human skin," Appl. Opt. **45**, 4174–4183 (2006).
8. M. E. Ramos and M. G. Lagorio, "True fluorescence spectra of leaves," Photochem. Photobiol. Sci. **3**, 1063–1066 (2004).
9. S. K. Chang, D. Arifler, R. Drezek, M. Follen, and R. Richards-Kortum, "Analytical model to describe fluorescence spectra of normal and preneoplastic epithelial tissue: comparison with Monte Carlo simulations and clinical measurements," J. Biomed. Opt. **9**, 511–522 (2004).
10. S. A. French, P. R. Territo, and R. S. Balaban, "Correction for inner filter effects in turbid samples: fluorescence assays of mitochondrial NADH," Am. J. Physiol. Cell Physiol. **275**, C900–C909 (1998).
11. C. M. Gardner, S. L. Jacques, and A. J. Welch, "Fluorescence spectroscopy of tissue: recovery of intrinsic fluorescence from measured fluorescence," Appl. Opt. **35**, 1780–1792 (1996).
12. C. M. Gardner, S. L. Jacques, and A. J. Welch, "Light transport in tissue: accurate expressions for one-dimensional fluence rate and escape function based upon Monte Carlo simulation," Lasers Surg. Med. **18**, 129–138 (1996).
13. J. C. Finlay and T. H. Foster, "Hemoglobin oxygen saturations in phantoms and *in vivo* from measurements of steady-state diffuse reflectance at a single, short source-detector separation," Med. Phys. **31**, 1949–1959 (2004).
14. N. N. Zhadin and R. R. Alfano, "Correction of the internal absorption effect in fluorescence emission and excitation spectra from absorbing and highly scattering media: theory and experiment," J. Biomed. Opt. **3**, 171–186 (1998).
15. T. Shakespeare and J. Shakespeare, "A fluorescent extension to the Kubelka–Munk model," Color Res. Appl. **28**, 4–14 (2003).
16. A. J. Durkin, S. Jaikumar, N. Ramanujam, and R. Richards-Kortum, "Relation between fluorescence spectra of dilute and turbid samples," Appl. Opt. **33**, 414–423 (1994).
17. W. E. Vargas and G. A. Niklasson, "Applicability conditions of the Kubelka–Munk theory," Appl. Opt. **36**, 5580–5586 (1997).
18. G. Yoon, S. A. Prahl, and A. J. Welch, "Accuracies of the diffusion approximation and its similarity relations for laser irradiated biological media," Appl. Opt. **28**, 2250–2255 (1989).
19. J. Wu, M. S. Feld, and R. P. Rava, "Analytical model for extracting intrinsic fluorescence in turbid media," Appl. Opt. **32**, 3585–3595 (1993).
20. J. Swartling, J. Svensson, D. Bengtsson, K. Terike, and S. Andersson-Engels, "Fluorescence spectra provide information on the depth of fluorescent lesions in tissue," Appl. Opt. **44**, 1934–1941 (2005).

21. N. Ghosh, S. K. Majumder, H. S. Patel, and P. K. Gupta, "Depth-resolved fluorescence measurement in a layered turbid medium by polarized fluorescence spectroscopy," Opt. Lett. **30**, 162–164 (2005).
22. Y. Wu, P. Xi, J. Y. Qu, T. H. Cheung, and M. Y. Yu, "Depth-resolved fluorescence spectroscopy reveals layered structure of tissue," Opt. Express **12**, 3218–3223 (2004).
23. S. K. Chang, D. Arifler, R. Drezek, M. Follen, and R. Richards-Kortum, "Analytical model to describe fluorescence spectra of normal and preneoplastic epithelial tissue: comparison with Monte Carlo simulations and clinical measurements," J. Biomed. Opt. **9**, 511–522 (2004).
24. R. L. Sheridan, K. T. Schomaker, L. C. Lucchina, J. Hurley, L. M. Yin, R. G. Tompkins, M. Jerath, A. Torri, K. W. Greaves, and D. P. Bua, "Burn depth estimation by use of indocyanine green fluorescence: initial human trial," J. Burn Care Res. **16**, 602–607 (1995).
25. S. Achilefu, R. B. Dorshow, J. E. Bugaj, and R. Rajagopalan, "Novel receptor-targeted fluorescent contrast agents for *in vivo* tumor imaging," Invest. Radiol. **35**, 479–485 (2000).
26. D. A. Hansen, A. M. Spence, T. Carski, and M. S. Berger, "Indocyanine green (ICG) staining and demarcation of tumor margins in a rat glioma model," Surg. Neurol. **40**, 451–456 (1993).
27. M. F. Modest, *Radiative Heat Transfer* (Academic, 2003).
28. L. G. Henyey and J. L. Greenstein, "Diffuse radiation in the galaxy," Ann. Astrophys. **93**, 70–83 (1940).
29. V. V. Tuchin, *Tissue Optics: Light Scattering Methods and Instruments for Medical Diagnosis* (SPIE Press, 2007).
30. M. J. C. Van Gemert, S. L. Jacques, H. Sterenborg, and W. M. Star, "Skin optics," IEEE Trans. Biomed. Eng. **36**, 1146–1154 (1989).
31. S. L. Jacques, C. A. Alter, and S. A. Prahl, "Angular dependence of He–Ne laser light scattering by human dermis," Lasers Life Sci. **1**, 309–333 (1987).
32. D. Q. Nguyen, R. Fedkiw, and H. W. Jensen, "Physically based modeling and animation of fire," in *Proceedings of the 29th Annual Conference on Computer Graphics and Interactive Techniques* (ACM New York, 2002), pp. 721–728.
33. S. Chandrasekhar, *Radiative Transfer* (Dover, 1960).
34. A. Ishimaru, *Wave Propagation and Scattering in Random Media* (Academic, 1978).
35. P. Kubelka and F. Munk, "A contribution to the optics of pigments," Z. Tech. Phys. **12**, 593–599 (1931).
36. M. J. C. van Gemert and W. M. Star, "Relations between the Kubelka–Munk and the transport equation models for anisotropic scattering," Lasers Life Sci. **1**, 287–298 (1987).
37. A. Gershun, "Fresnel reflection of diffusely incident light," J. Opt. Soc. Am. **35**, 162–162 (1945).
38. A. A. Kokhanovsky, "Radiative properties of optically thick fluorescent turbid media," J. Opt. Soc. Am. A **26**, 1896–1900 (2009).
39. T. H. Morton, "Fluorescent brightening agents on textiles: elementary optical theory and its practical applications," J. Soc. Dyers Colour. **79**, 238–242 (1963).
40. W. F. Cheong, S. A. Prahl, and A. J. Welch, "A review of the optical properties of biological tissues," IEEE J. Quantum Electron. **26**, 2166–2185 (1990).
41. J. H. Joseph, W. J. Wiscombe, and J. A. Weinman, "The Delta–Eddington approximation for radiative flux transfer," J. Atmos. Sci. **33**, 2452–2459 (1976).
42. D. Yudovsky and L. Pilon, "Simple and accurate expressions for diffuse reflectance of semi-infinite and two-layer absorbing and scattering media," Appl. Opt. **48**, 6670–6683 (2009).
43. R. R. Anderson and J. A. Parrish, "The optics of human skin," J. Invest. Dermatol. **77**, 13–19 (1981).
44. E. Salomatina, B. Jiang, J. Novak, and A. N. Yaroslavsky, "Optical properties of normal and cancerous human skin in the visible and near-infrared spectral range," J. Biomed. Opt. **11**, 064026 (2006).
45. C. R. Simpson, M. Kohl, M. Essenpreis, and M. Cope, "Near-infrared optical properties of *ex vivo* human skin and subcutaneous tissues measured using the Monte Carlo inversion technique," Phys. Med. Biol. **43**, 2465–2478 (1998).
46. L. Wang, S. L. Jacques, and L. Zheng, "CONV—Convolution for responses to a finite diameter photon beam incident on multi-layered tissues," Comput. Methods Programs Biomed. **54**, 141–150 (1997).
47. L. Wang and S. L. Jacques, "Monte Carlo modeling of light transport in multi-layered tissues in standard C," last accessed 3/31/2009, http://labs.seas.wustl.edu/bme/Wang/mcr5/Mcman.pdf.
48. K. J. Daniel, N. M. Laurendeau, and F. P. Incropera, "Prediction of radiation absorption and scattering in turbid water bodies," ASME J. Heat Transfer **101**, 63–67 (1979).